Chemical Science

ROYAL SOCIETY OF CHEMISTRY

EDGE ARTICLE

View Article Online
View Journal | View Issue

Cite this: *Chem. Sci.*, 2026, **17**, 1801

All publication charges for this article have been paid for by the Royal Society of Chemistry

Borate intercalation optimizes the electro-oxidation kinetics of α-$Ni(OH)_2$ nanosheets for selective electrochemical conversion of benzylamine to benzonitrile

Zhongcheng Wang,† Fengjuan Guo,† Xusheng Zhang, Hongtao Gao and Wenlong Yang *

Selective electrochemical oxidation of amine molecules presents a promising approach for synthesizing high-value nitrile products. Nevertheless, its practical implementation is largely impeded by the challenge in activating the dehydrogenation of $C(sp^3)$–H/$N(sp^3)$–H bonds in amines. In this work, borate anion intercalated α-$Ni(OH)_2$ (BI-$Ni(OH)_2$) nanosheets are synthesized *via* a convenient microwave-assisted synthesis strategy and employed as an exceptional electrocatalyst for the benzylamine (BA) oxidation reaction (BOR). Benefiting from its better wetting behavior, larger electroactive surface area and more favorable reaction kinetics, the BI-$Ni(OH)_2$ catalyst shows a distinctly enhanced activity in the electro-oxidation of BA to benzonitrile (BN) compared to pristine α-$Ni(OH)_2$ (P-$Ni(OH)_2$) nanosheets, especially giving rise to a faradaic efficiency exceeding 80% toward BN production at a voltage of 1.55 V, when coupled with the cathodic hydrogen evolution reaction (HER) in a two-electrode electrolyzer. Experimental measurements and density functional theory calculations conjointly demonstrate that borate intercalation not only reduces the energy barrier for generating NiOOH species as active centers, but also promotes the adsorption of BA molecules onto the catalyst surface, enabling significantly optimized electro-oxidation kinetics for the BOR, which is accountable for the enhanced electrocatalytic performance.

Received 19th June 2025
Accepted 21st November 2025

DOI: 10.1039/d5sc04502a

rsc.li/chemical-science

Introduction

Nitriles have been widely applied as a family of important chemical intermediates for industrial manufacturing of fine chemicals, dyes, and agrochemicals.[1–3] Considering the broad use of toxic HCN or metal cyanides in the traditional Sandmeyer reaction or nucleophilic substitution strategies, the consequent operation safety and waste emission problems largely limit their practical applications for nitrile production. On the other hand, although the electro-oxidation of primary amines with desirable atom economy seems to be an effective alternative route for synthesizing nitriles, such catalytic systems are usually implemented in organic solvents with the assistance of strong oxidants under high temperature and pressure conditions, inevitably leading to high energy consumption and serious environmental issues.[4–6] In this regard, selectively electro-oxidizing primary amines to nitriles has emerged as a safe, clean and energy-efficient strategy to address these challenges involved in the above-mentioned synthetic methods. Moreover, compared to the oxygen evolution reaction (OER), the electro-oxidation of primary amines is thermodynamically more favorable, which can replace the OER to promote the cathodic hydrogen evolution reaction (HER) for efficient hydrogen generation at lower potentials, offering great promise for sustainable organic chemical upgrading and concurrent green energy output.[7–10] However, due to the intrinsic inertness of C–H and N–H bonds with sp^3 hybridization in amines, the electrochemical amine-to-nitrile process generally suffers from sluggish electro-oxidation kinetics and heavily relies on the utilization of electrocatalysts to drive the conversion of amine C–N into nitrile C≡N bonds.[11,12] Therefore, it is of great importance to design and synthesize high-performance electrocatalysts for selectively electrooxidizing primary amines to nitriles with high energy conversion efficiency.

Recently, α-$Ni(OH)_2$ nanosheets with ultrathin two-dimensional (2D) layered configuration have been widely used as an excellent electrode material for energy storage and conversion, especially in the area of electrochemical organic synthesis because of their highly exposed electroactive surface and versatile catalytic capabilities.[13–15] Nevertheless, their electrocatalytic performance towards amine oxidation is largely

Key Laboratory of Optic-electric Sensing and Analytical Chemistry for Life Science, MOE, Key Laboratory of Analytical Chemistry for Life Science in Universities of Shandong, College of Chemistry and Molecular Engineering, Qingdao University of Science and Technology, Qingdao 266042, P. R. China. E-mail: wlyang@qust.edu.cn

† These authors contributed equally to this work.

limited by the inferior stability and low electrical conductivity, and is still far below the requirements of commercial application. Given that intercalating anions into layered structure materials has been demonstrated as one of the most promising amelioration strategies, which can not only enlarge their lamellar spacing to increase the contact area between the catalytic surface and the electrolyte, but also modify their electronic structures to regulate the electrochemical behaviors, thereby achieving significantly optimized electrocatalytic kinetics.[16–18] Among these selectable intercalation candidates, borate anions in the form of $B(OH)_4^-$ are very beneficial for the structural stability of hydroxide layers due to the robust bonding with metal ions. Furthermore, the intercalation of $B(OH)_4^-$ can effectively enhance the hydrophilicity of catalysts by virtue of the formation of hydrogen bonds with water molecules, contributing to OH^- adsorption and thus generating more active intermediates to promote the electrochemical process.[19,20] However, despite these favorable effects on the electrocatalytic activity derived from an intercalation engineering strategy, rare research has so far been focused on the underlying roles of intercalation anions in the electro-oxidation of amines, resulting in the comprehensive understanding of inherent relationships between them to be at an early stage. Furthermore, due to the elusive reaction pathways and accompanying surface reconstruction during the electrochemical oxidation process, the authentic activity origin of amine electro-oxidation on nickel-based catalysts is still ambiguous, which in turn impedes the further improvement of electrochemical performance from the viewpoint of mechanistic modulation.

In light of these considerations, a facile borate anion intercalation strategy was employed to enhance the electrocatalytic activity of ultrathin α-$Ni(OH)_2$ nanosheets for the benzylamine (BA) oxidation reaction (BOR). Moreover, taking the borate-intercalated α-$Ni(OH)_2$ nanosheets as an example, the efficacy of borate anions in the electro-oxidation of BA to benzonitrile (BN) was elaborately elucidated through combining experimental investigations and theoretical simulations. In particular, *in situ* infrared spectroscopy was performed to get molecular-level insights into the electrochemical oxidation pathway of BA to BN. As a result of synergetic effects between the enlarged electroactive area and optimized catalytic kinetics, borate-intercalated α-$Ni(OH)_2$ (denoted as BI-$Ni(OH)_2$) nanosheets show superior electrochemical BOR performance to pristine α-$Ni(OH)_2$ (denoted as P-$Ni(OH)_2$) nanosheets, giving an impressive faradaic efficiency (FE) of 80.74% for BN generation at a voltage of 1.55 V during the two-electrode electrolysis.

Results and discussion

In this study, both BI-$Ni(OH)_2$ and P-$Ni(OH)_2$ nanosheets were prepared by a simple microwave-assisted synthesis method as illustrated in Fig. 1A. The X-ray diffraction (XRD) pattern of P-$Ni(OH)_2$ nanosheets in Fig. 1B is in good agreement with the α-$Ni(OH)_2 \cdot 0.75H_2O$ phase (JCPDS Card No. 22-0444). Obviously, the position of the (001) peak at 7.3° for BI-$Ni(OH)_2$ nanosheets shows a negative shift compared to that for P-$Ni(OH)_2$ nanosheets (2θ = 11.3°), demonstrating the increased interlayer

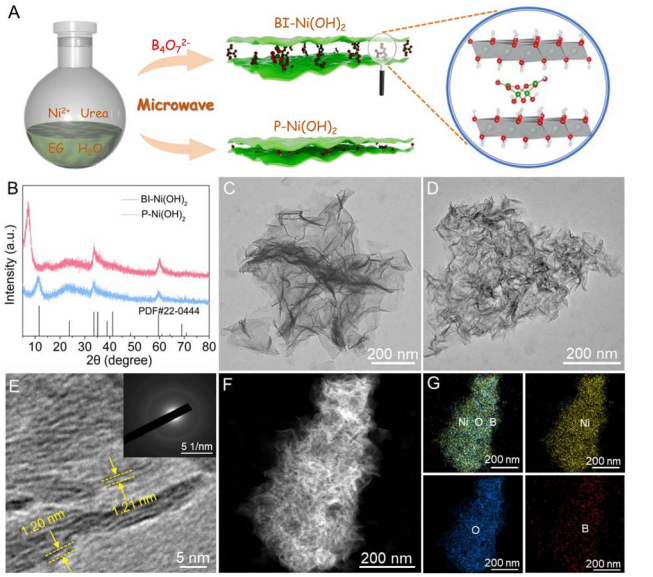

Fig. 1 (A) Schematic illustration of the synthesis of BI-$Ni(OH)_2$ and P-$Ni(OH)_2$ nanosheets. (B) XRD patterns of BI-$Ni(OH)_2$ and P-$Ni(OH)_2$ nanosheets. (C) TEM image of P-$Ni(OH)_2$ nanosheets. (D) TEM, (E) HRTEM (inset: the SAED pattern), (F) HAADF-STEM, and (G) EDX elemental mapping images of BI-$Ni(OH)_2$ nanosheets.

spacing of BI-$Ni(OH)_2$ nanosheets and therefore suggesting the successful intercalation of borate anions into $Ni(OH)_2$ interlayers. Here it is worth mentioning that the anion intercalation can give rise to evident structural disorder, which results in inevitable fluctuations in interlayer spacing and even the fracture of hydroxide layers.[21] In particular, based on Bragg's law,[22] the interlayer spacing of the (001) plane is calculated to be about 12.1 Å for BI-$Ni(OH)_2$ nanosheets. Taking into account the $Ni(OH)_2$ sheet thickness of 4.8 Å, the gallery height is thus estimated to be about 7.3 Å, close to the size value of the tetraborate anion (6.8 Å).[23] Hence, it can be safely inferred that the intercalated borate anions are present in the form of $B_4O_5(OH)_4^{2-}$. Transmission electron microscopy (TEM) images in Fig. 1C and D reveal that both the BI-$Ni(OH)_2$ and P-$Ni(OH)_2$ samples have similar sheet-like morphology with ultrathin thickness except that more wrinkles appear in the obtained nanosheets upon the intercalation of borate anions probably due to the presence of numerous structural disorders. The high-resolution TEM image of BI-$Ni(OH)_2$ nanosheets in Fig. 1E discloses the increased interlayer spacing of 12.1 Å, well consistent with the value concluded from the XRD analysis. Also, these discontinuous basal planes imply the weak crystallinity of BI-$Ni(OH)_2$ nanosheets with abundant structural disorders, which can be reflected by the feeble selected-area electron diffraction (SAED) pattern (see the inset of Fig. 1E). In addition, the high-angle annular dark-field scanning TEM (HAADF-STEM) and the corresponding elemental mapping images in Fig. 1F and G corroborate the co-existence and uniform distribution of Ni, O, and B elements in BI-$Ni(OH)_2$ nanosheets.

X-ray photoelectron spectroscopy (XPS) was conducted to survey the surface elemental composition and chemical state of

BI-Ni(OH)$_2$ nanosheets. The high-resolution Ni 2p spectra in Fig. 2A exhibit two distinct peaks at about 855.9 and 873.6 eV, indexed respectively, to the Ni 2p$_{3/2}$ and Ni 2p$_{1/2}$, and the spin-energy separation of 17.7 eV manifests that the oxidation state of Ni is predominantly +2.[24] Moreover, the O 1s XPS spectra in Fig. 2B can be deconvoluted into three types of oxygen. In particular, the peak at 531.2 eV is associated with the Ni–OH bond,[25] and the one at 532.5 eV is related to the C–OH or B–O bonds.[26,27] Meanwhile, the peak at 533.3 eV is attributed to the adsorbed water molecules.[28] As shown in Fig. 2C, the characteristic B 1s peak located at 191.9 eV matches well with the binding energy of the B–O bond, indicating the existence of borate anions.[19] Furthermore, Fourier transform infrared (FTIR) spectroscopy was performed to analyze the chemical compositions of the as-synthesized products. As depicted in Fig. 2D, for both Ni(OH)$_2$ nanosheets, two broad peaks at around 3357 and 1622 cm^{-1} are assigned to the O–H vibration of hydrogen-bonded hydroxyl groups and the bending mode of intercalated water molecules in the gallery space of α-Ni(OH)$_2$, respectively. Two weak bands at about 2970 and 2886 cm^{-1} along with a peak at 1053 cm^{-1} correspond respectively to the C–H and C–O vibrations of residual ethylene glycol, while a narrow peak at about 2178 cm^{-1} should be in association with the presence of OCN$^-$ anions due to the hydrolysis of urea during the synthetic procedure. Besides, the prominent peak at around 608 cm^{-1} can be ascribed to the δ_{OH} vibration.[29,30] Noteworthily, the appearance of three additional peaks at 1422, 1253 and 973 cm^{-1} indexed to the B–O stretching and B–OH in-plane bending vibrations fairly reconfirms the intercalation of borate anions in BI-Ni(OH)$_2$ nanosheets.[21,23] As reported before, the surface wettability of catalysts has a non-negligible influence on the overall electrocatalytic performance since catalytic reactions occur at the interface between the electrode and the electrolyte.[19,20] Therefore, the wetting behaviors of BI-Ni(OH)$_2$ and P-Ni(OH)$_2$ nanosheets were investigated by wettability measurements shown in Fig. 2E and F. As can be seen, P-Ni(OH)$_2$ nanosheets exhibit a large contact angle of 127.2°, revealing their poor surface wettability. By contrast, a smaller contact angle of 76.0° illustrates the better wetting behavior of BI-Ni(OH)$_2$ nanosheets, which unambiguously demonstrates that the intercalation of borate anions improves the hydrophilicity of Ni(OH)$_2$ nanosheets remarkably, offering desirable opportunities to facilitate electrolyte impregnation and consequently expedite the electrocatalytic process.

To evaluate the efficacy of borate intercalation on the BA oxidation, the electrochemical BOR performance of BI-Ni(OH)$_2$ and P-Ni(OH)$_2$ nanosheets was measured in 1.0 M KOH solution in the absence and presence of 25 mM BA in a typical three-electrode configuration. The linear sweep voltammetry (LSV) curves in Fig. 3A and S1 show that the anodic current densities increase substantially after the addition of 25 mM BA into 1.0 M KOH electrolyte, suggesting the favorable electrocatalytic response towards the BOR. Obviously, compared to P-Ni(OH)$_2$, the BI-Ni(OH)$_2$ electrode delivers a superior BOR activity in terms of its higher current density and lower onset potential (0.333 *vs.* 0.353 V *vs.* Ag/AgCl) for the BA oxidation (Fig. 3B), which can be comparable to other reported high-efficiency BOR catalysts (Table S1). Meanwhile, the corresponding Tafel plots in Fig. 3C reveal that the BI-Ni(OH)$_2$ electrode possesses a low Tafel slope of 13.0 mV dec^{-1}, smaller than that of the P-Ni(OH)$_2$ electrode (22.2 mV dec^{-1}), which implies the promoted BOR kinetics upon the intercalation of borate anions into Ni(OH)$_2$ nanosheets. Furthermore, the electrochemical impedance spectroscopy (EIS) was employed to study the interface behavior in the BOR process. As shown in Fig. 3D, the Nyquist plots recorded on the BI-Ni(OH)$_2$ electrode present a smaller semicircle diameter at high frequency, indicative of its lower charge-transfer resistance (R_{ct}) in comparison with the P-Ni(OH)$_2$ electrode, which implies better electron-transfer kinetics induced by the borate intercalation. All these results consistently demonstrate the positive role of borate intercalation in enhancing the electrocatalytic BOR activity of Ni(OH)$_2$ nanosheets. To get further insight into the oxidation products of the BOR, chronoamperometry tests were carried out at different potentials for 10 000 seconds on the BI-Ni(OH)$_2$ electrode. Subsequently, the collected oxidation products were qualitatively and quantitatively analyzed with a gas chromatography-

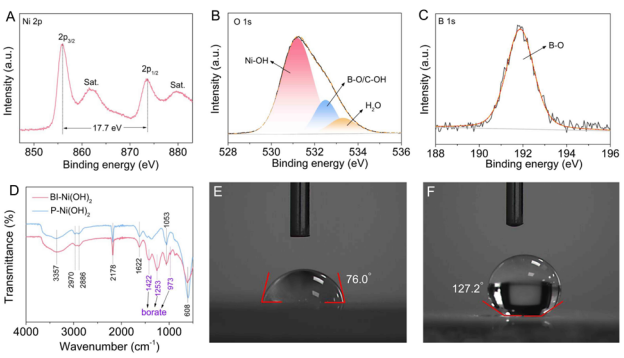

Fig. 2 (A) Ni 2p spectra, (B) O 1s spectra, and (C) B 1s spectra of BI-Ni(OH)$_2$ nanosheets. (D) FT-IR spectra of BI-Ni(OH)$_2$ and P-Ni(OH)$_2$ nanosheets. Water contact angle tests of (E) BI-Ni(OH)$_2$ and (F) P-Ni(OH)$_2$ nanosheets.

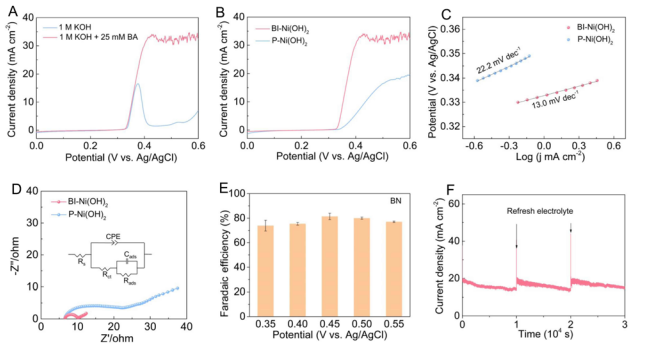

Fig. 3 (A) LSV curves of BI-Ni(OH)$_2$ obtained at a scan rate of 5 mV s^{-1} in 1.0 M KOH without and with 25 mM BA. (B) LSV curves, (C) Tafel plots, and (D) Nyquist plots of BI-Ni(OH)$_2$ and P-Ni(OH)$_2$ catalysts measured in 1.0 M KOH with 25 mM BA and the corresponding equivalent circuit (inset). (E) The calculated FEs for BN production on the BI-Ni(OH)$_2$ catalyst at various potentials. (F) The electrocatalytic stability of BI-Ni(OH)$_2$ for the BOR at 0.40 V *versus* Ag/AgCl in 1.0 M KOH with 25 mM BA.

mass spectrometer (GC-MS). As revealed in Fig. S2 and 3E, the oily BN is the main product after the BA electro-oxidation at various potentials ranging from 0.35 to 0.55 V *versus* Ag/AgCl. In detail, the corresponding faradaic efficiencies (FEs) for BN production at 0.35, 0.40, 0.45, 0.50 and 0.55 V *versus* Ag/AgCl are estimated respectively to be about 73.88%, 75.39%, 81.40%, 80.00%, and 76.97%, representing good selectivity for the conversion of BA to BN on the BI-Ni(OH)$_2$ electrode. Next, the electrochemical stability of the BI-Ni(OH)$_2$ electrode for the BOR was assessed in 1.0 M KOH in the presence of 25 mM BA at a potential of 0.40 V *versus* Ag/AgCl. In Fig. 3F, the chronoamperometry curve exhibits gradual attenuation in the current density arising from the BA consumption in each cycling test. It should be noted that the current density can be immediately regained after replacing the electrolyte, suggesting its satisfactory electrochemical stability for the BA oxidation. In addition, as can be seen from the XRD and TEM results in Fig. S3, both the BOR activity and pristine structure of BI-Ni(OH)$_2$ nanosheets were basically retained even undergoing three successive cycling tests, jointly indicating the excellent electrocatalytic durability for the BOR.

Considering the remarkable BOR activity of BI-Ni(OH)$_2$ nanosheets, the selective electro-oxidation of BA to BN was further paired with cathodic H_2 production in a two-electrode electrolyzer equipped with an anion exchange membrane, as illustrated schematically in Fig. 4A. From the LSV curves in Fig. 4B, it can be observed that both the anodic and cathodic currents increase sharply after the addition of 25 mM BA into the anodic electrolyte, suggesting that the HER process can be distinctly promoted when coupled with the BA electro-oxidation. Next, voltage-dependent electrolysis measurements were implemented for 10 000 seconds to evaluate the electrochemical performance for BN and H_2 production in such a hybrid electrolyzer. Impressively, as shown in Fig. 4C, the FEs for H_2 production reach up to about 100% at voltages ranging from 1.50–1.65 V; meanwhile, the FE for BN production can exceed 80% at a voltage of 1.55 V, revealing its satisfactory BA-to-BN selectivity along with high energy conversion efficiency for H_2 production, which may create potential opportunities for future applications in industry. To further gain molecular-level insights into the BOR pathway, *in situ* FT-IR spectroscopy was carried out at varying potentials to probe the intermediates and oxidation products on BI-Ni(OH)$_2$ in a three-electrode system. As shown in Fig. 4D, a peak can be detected at around 2375 cm^{-1}, corresponding to the dissolved CO_2.[31,32] Besides, a prominent peak located at around 2180 cm^{-1} is associated with the presence of OCN^- anions as mentioned in Fig. 2D. Of note, the absorption peaks positioned at 1622 and 2235 cm^{-1} are ascribed to the symmetric bending vibration of the C=N bond in imine intermediates and the stretching vibration of the C≡N bond in the as-formed BN molecules, respectively.[33,34] Obviously, the two peaks become more positive with the gradual increase of potential, demonstrating the progressive electro-oxidation of the C–H and N–H bonds and thereby the subsequent formation of nitrile groups during the BOR process, which undoubtedly highlights the selective conversion of BA to BN over the BI-Ni(OH)$_2$ electrode.

To deeply decipher the contribution of borate intercalation to the enhanced BOR activity, a series of electrochemical tests (three-electrode configuration) together with density functional theory (DFT) calculations were executed. As shown in Fig. S4 and 5A, the electrochemical active surface areas (ECSAs) of BI-Ni(OH)$_2$ and P-Ni(OH)$_2$ electrodes were assessed by a double-layer capacitance (C_{dl}) method. Compared with P-Ni(OH)$_2$ (0.25 mF cm^{-2}), BI-Ni(OH)$_2$ exhibits a larger C_{dl} value of 0.41 mF cm^{-2}, signifying its more exposed active sites because of the

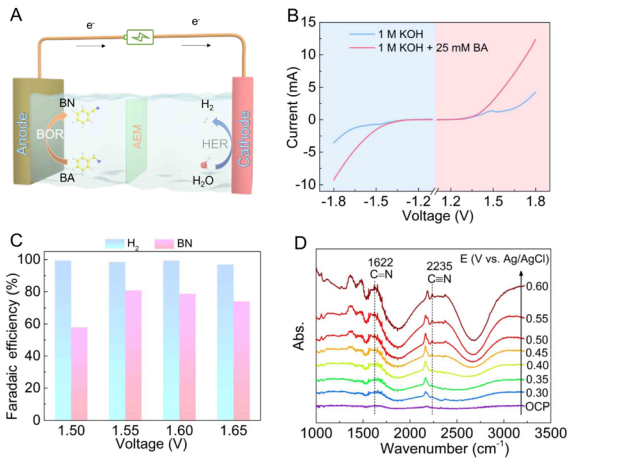

Fig. 4 (A) Schematic illustration of the BOR paired with the HER over a two-electrode electrolyzer. (B) LSV curves recorded at a scan rate of 5 mV s^{-1} in 1.0 M KOH with and without 25 mM BA. (C) The calculated FEs for H_2 and BN production at different voltages in the two-electrode electrolyzer. (D) Potential-dependent *in situ* FT-IR spectra of the BI-Ni(OH)$_2$ catalyst in 1.0 M KOH with 25 mM BA.

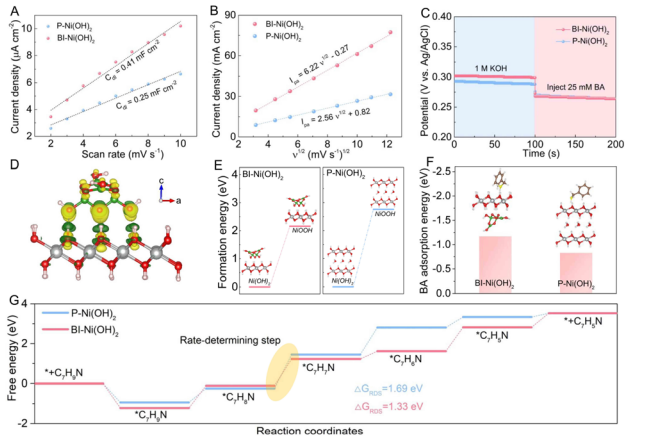

Fig. 5 (A) C_{dl} values and (B) linear correlations between the anodic peak current density and the square root of the scan rate for BI-Ni(OH)$_2$ and P-Ni(OH)$_2$ obtained in 1.0 M KOH. (C) OCP tests for BI-Ni(OH)$_2$ and P-Ni(OH)$_2$ before and after injecting 25 mM BA into 1.0 M KOH electrolyte. (D) The charge density difference of BI-Ni(OH)$_2$, where the isosurface value is set to 0.005 e Å^{-3}. The green and yellow regions represent charge depletion and accumulation, respectively. (E) The calculated NiOOH formation energies and (F) BA adsorption energies for BI-Ni(OH)$_2$ and P-Ni(OH)$_2$. (G) The energy profiles for the electro-oxidation of BA to BN on BI-Ni(OH)$_2$ and P-Ni(OH)$_2$ surfaces.

enlarged interlayer spacing arising from borate intercalation. Also, LSV curves for the BOR were normalized by their corresponding C_{dl} values (Fig. S5), revealing that BI-Ni(OH)$_2$ has higher intrinsic catalytic activity towards BA electro-oxidation. It has been previously reported that the electrophilic NiOOH intermediates derived from an electrochemical dehydrogenation reaction of Ni(OH)$_2$ catalysts are generally considered as the activity origins for the nucleophile electro-oxidation.[35,36] In this regard, the electrochemical redox properties of BI-Ni(OH)$_2$ and P-Ni(OH)$_2$ electrodes were evaluated from CV curves at different scan rates in 1.0 M KOH solution (Fig. S6). Evidently, the intensity of the oxidation peak becomes stronger with the increase of the scan rate, in particular, showing a good linear relationship with the square root of scan rates in Fig. 5B. Comparatively, the linear slope for BI-Ni(OH)$_2$ is much higher than that for P-Ni(OH)$_2$, indicating that the borate intercalation endows Ni(OH)$_2$ nanosheets with superior dehydrogenation ability to form more electroactive NiOOH species for subsequent BA electro-oxidation. In addition, open-circuit potential (OCP) measurements were conducted to survey the adsorption behavior of BA molecules in the Helmholtz layer. By comparing the OCP curves in Fig. 5C, BI-Ni(OH)$_2$ presents a more significant decline of OCP after injecting 25 mM BA into 1.0 M KOH solution with respect to P-Ni(OH)$_2$, which verifies that the intercalation of borate anions is conducive to ameliorating the adsorption capacity of Ni(OH)$_2$ nanosheets to BA molecules.[34] To theoretically reveal the charge transfer between the intercalated borate anions and Ni(OH)$_2$, the charge density difference was calculated (Fig. 5D). It can be seen that the charge accumulates on the borate anion side and depletes near the Ni(OH)$_2$ region, suggesting that the electrons flow from Ni(OH)$_2$ to borate anions. Subsequently, the Bader charge analysis confirms that there are 1.11 electrons transferred from Ni(OH)$_2$ to the borate anion. Therefore, an electron-deficient surface is formed on the Ni(OH)$_2$ side, which may contribute to the adsorption of the electron-rich amine group in BA molecules.[11] Moreover, the energy required for the dehydrogenation reaction from Ni(OH)$_2$ to NiOOH species was calculated based on the theoretical models in Fig. S7 and S8. As shown in Fig. 5E and Table S2, the NiOOH formation energy for BI-Ni(OH)$_2$ nanosheets is about 2.16 eV, which is obviously smaller than that for P-Ni(OH)$_2$ nanosheets (2.76 eV), meaning that the generation of as-aforementioned NiOOH species proceeds more easily on the BI-Ni(OH)$_2$ catalyst, in accordance with the experimental result. Simultaneously, compared to P-Ni(OH)$_2$ (-0.83 eV) in Fig. 5F, S9 and Table S2, the lower BA adsorption energy of BI-Ni(OH)$_2$ (-1.17 eV) demonstrates that the adsorption of BA molecules is energetically more beneficial onto the as-formed NiOOH site on the BI-Ni(OH)$_2$ surface, providing a theoretical support for the promoted BA adsorption kinetics owing to the borate intercalation. Besides, the complete BA oxidation routes on BI-Ni(OH)$_2$ and P-Ni(OH)$_2$ catalysts were investigated by DFT simulations. As observed from the Gibbs free energy difference (ΔG) in Fig. 5G, Tables S3 and S4, the transformation of *C_7H_8N to the *C_7H_7N intermediate is the rate-determining step (RDS) for both of the two catalyst models because this step has the largest energy barrier along this reaction pathway.[37] Especially, the ΔG value of the RDS for BI-Ni(OH)$_2$ is found to be 1.33 eV, lower than that for P-Ni(OH)$_2$ (1.69 eV), unequivocally indicating that the borate intercalation can significantly reduce the RDS energy barrier to expedite the electrochemical BOR kinetics from the viewpoint of reaction pathway modulation.

Conclusions

In summary, structurally-new BI-Ni(OH)$_2$ nanosheets featuring borate anions ($B_4O_5(OH)_4^{2-}$) intercalated into the interlayer of α-Ni(OH)$_2$ nanosheets were put forward as a desirable catalyst for the selective electro-oxidation of BA to BN. Furthermore, the crucial efficacy of borate intercalation in the electrocatalytic BOR process was elucidated experimentally and theoretically by taking the BI-Ni(OH)$_2$ catalyst as a proof-of-concept prototype. It is found that the unique intercalation of borate anions endows α-Ni(OH)$_2$ with enlarged layer spacing and enhanced hydrophilicity, rendering it more advantageous for electrolyte impregnation. Electrochemical tests together with DFT calculations reveal that ultrathin BI-Ni(OH)$_2$ nanosheets are more favorable for both the formation of electroactive NiOOH species and the adsorption of BA molecules, affording optimized electro-oxidation kinetics for the BOR. As a result, the obtained BI-Ni(OH)$_2$ catalyst shows a higher electrocatalytic BOR activity with respect to the pristine counterpart, achieving a FE of 81.40% for BN generation at a potential of 0.45 V *vs.* Ag/AgCl. Specifically, when coupled with the HER in a two-electrode electrolyzer, the FEs for BN and H_2 generation can reach 80% and 100% at a low voltage of 1.55 V, respectively. This work provides an effective strategy for facilitating the reaction kinetics toward BA electro-oxidation.

Experimental

Materials

All reagents were of analytical reagent grade, purchased from Sinopharm Chemical Reagent Co., Ltd, and used as received without further purification.

Preparation of BI-Ni(OH)$_2$ nanosheets

In a typical process, $NiCl_2 \cdot 6H_2O$ (1 mmol), $Na_2B_4O_7 \cdot 10H_2O$ (1 mmol) and urea (4 mmol) were fully dissolved in a mixture of ethylene glycol (35 mL) and water (5 mL) under vigorous stirring at room temperature. Subsequently, the resulting mixture was heated at 140 °C for 30 minutes under microwave irradiation (600 W) in a microwave reflux system. Afterward, the product was washed several times with deionized water and anhydrous ethanol, and then dried at 65 °C for further characterization.

Preparation of P-Ni(OH)$_2$ nanosheets

The preparation of P-Ni(OH)$_2$ nanosheets is similar to that of BI-Ni(OH)$_2$ nanosheets, except that 1 mmol of $Na_2B_4O_7 \cdot 10H_2O$ was not added during the synthesis process.

Characterization

X-ray diffraction patterns (XRD) were recorded on a Japan Rigaku D/max-rA equipped with graphite monochromatized high-intensity Cu Kα radiation ($\lambda = 1.54178$ Å). Transmission electron microscopy (TEM) and high-resolution transmission electron microscopy (HRTEM) were carried out on a JEOL-2010 TEM at an acceleration voltage of 200 kV. High-angle annular dark-field scanning transmission electron microscopy (HAADF-STEM) and the corresponding mapping test were performed on a JEOL JEM-ARF200F TEM/STEM. X-ray photoelectron spectroscopy (XPS) was performed on an ESCALAB MKII X-ray photoelectron spectrometer with an excitation source of Mg Kα = 1253.6 eV. Fourier transform infrared (FT-IR) spectroscopy, with a scanning range from 4000 to 400 cm^{-1}, was conducted on a NICOLET FT-IR spectrometer using KBr pellets at room temperature.

Potential-dependent *in situ* FT-IR spectroscopy was performed on a Thermo Scientific Nicolet 6700 FT-IR spectrometer equipped with an attenuated total reflection (ATR) configuration applying a liquid nitrogen cooled MCT-A detector. In this test, all data were recorded in a three-electrode system by employing a graphite rod and a saturated Ag/AgCl electrode as the counter electrode and the reference electrode, respectively. A glassy carbon electrode (GCE, 6 mm in diameter) with catalysts (about 0.15 mg) was used as the working electrode, which was pressed against a CaF_2 crystal with a thickness of 2 mm. The FT-IR spectral resolution was set to 4.0 cm^{-1} with 32 scans per spectrum. The incident beam angle was set to 60°. The data at varying potentials were recorded after 60 s of electrolysis in 1.0 M KOH containing 25 mM BA.

Electrochemical measurements

All of the electrochemical tests were conducted on a CHI660B electrochemical station. For the three-electrode system, a graphite rod and a saturated Ag/AgCl electrode were used as the counter electrode and the reference electrode, respectively. A GCE (5 mm in diameter) with different catalysts was applied as the working electrode. Typically, 30 μL of Nafion solution (5 wt%) and 4 mg of the catalyst were ultrasonically dispersed into a water-isopropanol solution (1 mL, volume ratio of 3 : 1). After that, 15 μL of the resulting catalyst ink was uniformly loaded onto a GCE, which was dried naturally at room temperature. Linear sweep voltammetry (LSV) was performed at a scan rate of 5 mV s^{-1} in 1.0 M KOH without and with 25 mM BA. Electrochemical impedance spectroscopy (EIS) was performed in 1.0 M KOH with 25 mM BA at 0.40 V *vs.* Ag/AgCl, during which the frequency range was 100 K Hz to 1 Hz and the amplitude of the applied voltage was set to 5 mV. The electrochemical stability test was conducted at a potential of 0.40 V *vs.* Ag/AgCl in 1.0 M KOH containing 25 mM BA. For the two-electrode system, the electrochemical measurements were conducted in an H-type cell with an anion exchange membrane (Fumasep FAB-PK-130). A Pt electrode was used as the counter electrode, and 50 μL of the resulting catalyst ink loaded onto carbon paper (1 cm × 1 cm) was used as the working electrode.

Author contributions

Z. C. Wang: investigation, validation, data curation, writing-original draft. F. J. Guo: theoretical calculation, validation. X. S. Zhang: investigation. H. T. Gao: software, supervision. W. L. Yang: conceptualization, validation, resources, supervision, writing-original draft, writing-review & editing.

Conflicts of interest

There are no conflicts to declare.

Data availability

The data supporting this article have been included as part of the supplementary information (SI). Supplementary information: product characterization, theoretical calculations, catalyst characterization (XRD, TEM), and electrochemical measurements. See DOI: **https://doi.org/10.1039/d5sc04502a**.

Acknowledgements

This work was supported by the National Natural Science Foundation of China (21805149) and the Natural Science Foundation of Shandong Province of China (ZR2018BB012).

Notes and references

1 R. Y. Liu, M. Bae and S. L. Buchwald, *J. Am. Chem. Soc.*, 2018, **140**, 1627–1631.
2 J. Kim, G. Golime, H. Y. Kim and K. Oh, *Asian J. Org. Chem.*, 2019, **8**, 1674–1679.
3 P. Anbarasan, T. Schareina and M. Beller, *Chem. Soc. Rev.*, 2011, **40**, 5049.
4 H. H. Hodgson, *Chem. Rev.*, 1947, **40**, 251–277.
5 K. K. Sun, J. L. Sun, G. P. Lu and C. Cai, *Green Chem.*, 2019, **21**, 4334–4340.
6 Y. X. Sun, H. Shin, F. Y. Wang, B. L. Tian, C. W. Chiang, S. T. Liu, X. S. Li, Y. Q. Wang, L. Y. Tang, W. A. Goddard and M. N. Ding, *J. Am. Chem. Soc.*, 2022, **144**, 15185–15192.
7 M. M. Song, M. M. Feng, F. Li, S. S. Lv, Y. Zhou and Z. Chen, *Inorg. Chem.*, 2024, **63**, 15215–15223.
8 Y. Li, Y. Q. Jiao, H. J. Yan, G. C. Yang, Y. Liu, C. G. Tian, A. P. Wu and H. G. Fu, *Angew. Chem., Int. Ed.*, 2023, **62**, e202306640.
9 L. Z. Sun, Z. Y. Zhou, Y. N. Xie, J. G. Zheng, X. Pan, L. N. Li and G. H. Zhao, *Adv. Funct. Mater.*, 2023, **33**, 2301884.
10 F. H. Ma, S. H. Wang, L. Y. Han, Y. H. Guo, Z. Y. Wang, P. Wang, Y. Y. Liu, H. F. Cheng, Y. Dai, Z. K. Zheng and B. B. Huang, *ACS Appl. Mater. Interfaces*, 2021, **13**, 56140–56150.
11 W. B. Wang, Y. T. Wang, R. O. Yang, Q. L. Wen, Y. W. Liu, Z. Jiang, H. Q. Li and T. Y. Zhai, *Angew. Chem., Int. Ed.*, 2020, **59**, 16974–16981.
12 L. Chen, Z. H. Yin, J. Y. Cui, C. Q. Li, K. P. Song, H. Liu and J. J. Wang, *J. Am. Chem. Soc.*, 2024, **146**, 27090–27099.

13 Q. He, Y. Y. Wan, H. L. Jiang, Z. W. Pan, C. Q. Wu, M. Wang, X. J. Wu, B. J. Ye, P. M. Ajayan and L. Song, *ACS Energy Lett.*, 2018, **3**, 1373–1380.
14 G. B. Chen, X. D. Li and X. L. Feng, *Angew. Chem., Int. Ed.*, 2022, **61**, e202209014.
15 M. R. Gao, W. C. Sheng, Z. B. Zhuang, Q. R. Fang, S. Gu, J. Jiang and Y. S. Yan, *J. Am. Chem. Soc.*, 2014, **136**, 7077–7084.
16 M. Ma, R. X. Ge, X. Q. Ji, X. Ren, Z. Liu, A. M. Asiri and X. P. Sun, *ACS Sustainable Chem. Eng.*, 2017, **5**, 9625–9629.
17 Y. Yu, W. Zhou, X. H. Zhou, J. S. Yuan, X. W. Zhang, X. X. Meng, F. Sun, J. H. Gao and G. B. Zhao, *Adv. Funct. Mater.*, 2025, **35**, 2419871.
18 Y. L. Meng, Y. Q. Li, Z. Tan, X. Chen, L. L. Wu, L. W. Ji, Q. S. Wang, X. Z. Song and S. Song, *Energy Fuels*, 2021, **35**, 2775–2784.
19 T. Q. Gao, Y. Q. Zhou, X. J. Zhao, Z. H. Liu and Y. Chen, *Adv. Funct. Mater.*, 2024, **34**, 2315949.
20 W. Wang, T. Q. Gao, X. Y. Li, J. W. Liu, X. J. Zhao and Z. H. Liu, *ACS Appl. Nano Mater.*, 2025, **8**, 4670–4679.
21 Y. F. Xin, X. Dai, G. J. Lv, X. D. Wei, S. Li, Z. Q. Li, T. Xue, M. Shi, K. Y. Zou, Y. Z. Chen and Y. N. Liu, *ACS Appl. Mater. Interfaces*, 2021, **13**, 28118–28128.
22 Z. N. Li, S. Gadipelli, H. C. Li, C. A. Howard, D. J. L. Brett, P. R. Shearing, Z. X. Guo, I. P. Parkin and F. Li, *Nat. Energy*, 2020, **5**, 160–168.
23 L. S. Li, S. J. Ma, X. S. Liu, Y. Yue, J. B. Hui, R. R. Xu, Y. M. Bao and J. Rocha, *Chem. Mater.*, 1996, **8**, 204–208.
24 Y. Tong, P. Z. Chen, M. X. Zhang, T. P. Zhou, L. D. Zhang, W. S. Chu, C. Z. Wu and Y. Xie, *ACS Catal.*, 2018, **8**, 1–7.
25 D. J. Zheng, M. Görlin, K. McCormack, J. Kim, J. Y. Peng, H. B. Xu, X. X. Ma, J. M. LeBeau, R. A. Fischer, Y. Román-Leshkov and Y. Shao-Horn, *Chem. Mater.*, 2023, **35**, 5017–5031.
26 Y. X. Jiang, C. Y. Ji, J. J. Wu, Q. R. Han, C. Cui, W. Q. Shi and Z. L. Peng, *Polymer*, 2022, **243**, 124625.
27 W. J. Jiang, S. Niu, T. Tang, Q. H. Zhang, X. Z. Liu, Y. Zhang, Y. Y. Chen, J. H. Li, L. Gu, L. J. Wan and J. S. Hu, *Angew. Chem., Int. Ed.*, 2017, **56**, 6572–6577.
28 Z. P. Wu, S. W. Zuo, Z. H. Pei, J. Zhang, L. R. Zheng, D. Y. Luan, H. B. Zhang and X. W. Lou, *Sci. Adv.*, 2025, **11**, eadu5370.
29 D. D. Jia, H. Y. Gao, W. J. Dong, S. Fan, R. Dang and G. Wang, *ACS Appl. Mater. Interfaces*, 2017, **9**, 20476–20483.
30 L. P. Xu, Y. S. Ding, C. H. Chen, L. L. Zhao, C. Rimkus, R. Joesten and S. L. Suib, *Chem. Mater.*, 2008, **20**, 308–316.
31 Y. Hao, D. S. Yu, S. Q. Zhu, C. H. Kuo, Y. M. Chang, L. Q. Wang, H. Y. Chen, M. H. Shao and S. J. Peng, *Energy Environ. Sci.*, 2023, **16**, 1100–1110.
32 L. F. Fan, Y. X. Ji, G. X. Wang, J. X. Chen, K. Chen, X. Liu and Z. H. Wen, *J. Am. Chem. Soc.*, 2022, **144**, 7224–7235.
33 Z. T. Tu, X. Y. He, X. Liu, D. K. Xiong, J. Zuo, D. L. Wu, J. Y. Wang and Z. F. Chen, *Chin. J. Catal.*, 2024, **58**, 146–156.
34 L. Y. Zeng, W. B. Chen, Q. H. Zhang, S. Z. Xu, W. Y. Zhang, F. Lv, Q. Z. Huang, S. G. Wang, K. Yin, M. G. Li, Y. Yang, L. Gu and S. J. Guo, *ACS Catal.*, 2022, **12**, 11391–11401.
35 B. Zhou, Y. Y. Li, Y. Q. Zou, W. Chen, W. Zhou, M. L. Song, Y. J. Wu, Y. X. Lu, J. L. Liu, Y. Y. Wang and S. Y. Wang, *Angew. Chem., Int. Ed.*, 2021, **60**, 22908–22914.
36 W. Chen, C. Xie, Y. Y. Wang, Y. Q. Zou, C. L. Dong, Y. C. Huang, Z. H. Xiao, Z. X. Wei, S. Q. Du, C. Chen, B. Zhou, J. M. Ma and S. Y. Wang, *Chem*, 2020, **6**, 2974–2993.
37 V. T. T. Phan, Q. P. Nguyen, B. Wang and I. J. Burgess, *J. Am. Chem. Soc.*, 2024, **146**, 4830–4841.